

Scalable Fabrication of Stable High Efficiency Perovskite Solar Cells and Modules Utilizing Room Temperature Sputtered SnO₂ Electron Transport Layer


Longbin Qiu, Zonghao Liu, Luis K. Ono, Yan Jiang, Dae-Yong Son, Zafer Hawash, Sisi He, and Yabing Qi*

Stability and scalability have become the two main challenges for perovskite solar cells (PSCs) with the research focus in the field advancing toward commercialization. One of the prerequisites to solve these challenges is to develop a cost-effective, uniform, and high quality electron transport layer that is compatible with stable PSCs. Sputtering deposition is widely employed for large area deposition of high quality thin films in the industry. Here the composition, structure, and electronic properties of room temperature sputtered SnO₂ are systematically studied. Ar and O₂ are used as the sputtering and reactive gas, respectively, and it is found that a highly oxidizing environment is essential for the formation of high quality SnO₂ films. With the optimized structure, SnO₂ films with high quality have been prepared. It is demonstrated that PSCs based on the sputtered SnO₂ electron transport layer show an efficiency up to 20.2% (stabilized power output of 19.8%) and a T₈₀ operational lifetime of 625 h. Furthermore, the uniform and thin sputtered SnO₂ film with high conductivity is promising for large area solar modules, which show efficiencies over 12% with an aperture area of 22.8 cm² fabricated on 5 × 5 cm² substrates (geometry fill factor = 91%), and a T₈₀ operational lifetime of 515 h.

1. Introduction

Perovskite solar cells (PSCs) have attracted much attention from both academia and industry due to their high performance and low cost. Certified efficiency for small area cell has reached 23.3%.^[1] So far more and more efforts are directed towards

Dr. L. Qiu, Dr. Z. Liu, Dr. L. K. Ono, Dr. Y. Jiang, Dr. D.-Y. Son, Dr. Z. Hawash, Dr. S. He, Prof. Y. B. Qi
Energy Materials and Surface Sciences Unit (EMSSU)
Okinawa Institute of Science and Technology Graduate University (OIST)
1919-1 Tancha, Kunigami-gun, Onna-son, Okinawa 904-0495, Japan
E-mail: Yabing.Qi@OIST.jp

 The ORCID identification number(s) for the author(s) of this article can be found under <https://doi.org/10.1002/adfm.201806779>.

© 2019 The Authors. Published by WILEY-VCH Verlag GmbH & Co. KGaA, Weinheim. This is an open access article under the terms of the Creative Commons Attribution-NonCommercial-NoDerivs License, which permits use and distribution in any medium, provided the original work is properly cited, the use is non-commercial and no modifications or adaptations are made.

The copyright line for this article was changed on 11 November 2019 after original online publication.

DOI: 10.1002/adfm.201806779

the commercialization of perovskite solar cells.^[2] However, there are still two main challenges, i.e., long-term device operational stability and large scale fabrication. The device instability issue is complicated, being affected by the intrinsic stability of perovskite materials,^[3] electron transport layer (ETL),^[4] hole transport layer,^[5] electrode materials,^[6] and the interfaces between the perovskite layer and charge transport layers.^[7] It has been proposed that the most widely used ETL TiO₂ is one of the important factors responsible for light-induced degradation of perovskite solar cells.^[8] SnO₂ is a promising candidate to replace TiO₂, and a highest certified efficiency of 21.52% has been achieved for a planar junction structure PSC using SnO₂ ETL.^[9] Compared with TiO₂, SnO₂ possesses several advantages such as higher mobility and better energy level alignment.^[10] More importantly, use of SnO₂ as ETL can eliminate/minimize

degradation of perovskite solar cells induced by TiO₂ ETL, leading to significantly enhanced operational lifetime under continuous light illumination. In a recent work for interface tailoring, unencapsulated perovskite solar cells based on SnO₂ ETL indeed show much longer lifetime compared with cells based on TiO₂ ETL and a much smaller burn in loss.^[11]

The second challenge is regarding fabrication of large scale perovskite solar modules (PSMs) with performance comparable to what has been achieved for small area cells.^[2] With the development of large scale deposition of high quality perovskite films, there are an increasing number of reports about PSMs.^[12] The certified efficiency has reached 16.0% with an aperture area of 16.29 cm².^[1a] With an advanced solvent and vacuum free process for perovskite films, PSMs with a larger aperture area of 36.1 cm² reached a certified efficiency of 12.1%.^[13] Other than the perovskite layer, low-cost and large scale deposition of ETL is equally important.^[2] So far most PSMs have been fabricated using TiO₂ ETL, which requires high temperature processing and also results in instability issues.^[14] Furthermore, due to the high resistance of TiO₂, a complicated laser patterning process is required to remove the coated TiO₂ layer in the interconnection area between each subcell to ensure good contact for series connection.^[15] Without removing the TiO₂ layer in the

interconnection can significantly increase series resistance and lower PSM performance.^[16] In contrast with TiO₂, SnO₂ could be easily coated by low temperature solution process,^[10a,17] electrodeposition process,^[18] atomic layer deposition,^[19] chemical bath deposition,^[20] electron-beam deposition,^[21] and sputtering deposition.^[22] However, most of the reported results based on SnO₂ ETL are small area devices and large area PSMs are rare.^[14] Among these different types of technology, sputtering deposition is promising for large scale, low-cost, and uniform deposition with the use of low-cost SnO₂ target. To date there are only two reports using sputtering of SnO₂ for perovskite solar cells, but the reported efficiency is only 14% for an area of 0.09 cm² due to the unoptimized structure.^[23] Besides the better uniformity across large area achieved by sputtering deposition, the higher conductivity of SnO₂ compared with TiO₂ can also help improve the interconnection between sub-cells in PSMs. Although use of SnO₂ as ETL in perovskite solar cells has shown some initial success, it remains elusive regarding how its morphology, composition, and crystallinity affect the device performance. Furthermore, the current high efficiency perovskite solar cells based on SnO₂ ETL use spin coated SnO₂ with a small thickness of 25 nm, which can cause issues (e.g., fringe effects, pinholes, film thickness variation across a large area, etc.) when upscaling from small solar cells to large solar modules.

Here we report a study on room temperature sputtered SnO₂ ETL for high-efficiency and stable perovskite solar cells and modules. The efficiency for small area cells reaches 20.2%, with 19.8% stabilized power output, in a planar structure. We show that the surface morphology, composition, and surface traps state (–OH) are critical for fabrication of high performance devices. A highly oxidizing environment is key to obtaining high quality SnO₂ films. Our ultraviolet photoemission spectroscopy (UPS) results show that with prolonged sputtering time and higher Ar gas ratio, Ar sputtering can induce more tail states above the valance band, which increases charge recombination thus lowers open-circuit voltage (*V*_{OC}). Crystallinity is not a determining factor for device performance. These SnO₂ films are deposited under room temperature and are amorphous, with an optimized thickness in the range of 10–20 nm. The operational stability of perovskite devices based on such SnO₂ films shows a *T*₈₀ lifetime of 625 h (350 h including the initial exponential loss). Due to the high conductivity of SnO₂, high performance and stable modules are fabricated without removing the ETL in the interconnection area when patterning. For the first time mini-modules based on the SnO₂ ETL with an aperture area of 22.8 cm² and six cells in series connection have been fabricated demonstrating an efficiency over 12%.

2. Results and Discussion

The film quality of the sputtered SnO₂ is mainly determined by the deposition conditions and is systematically optimized for perovskite solar cells in this work. SnO₂ is generally an n-type semiconductor due to the existence of intrinsic defects such as oxygen vacancies and tin interstitials.^[24] On the other hand, the Sn²⁺ related oxide SnO exhibits p-type properties and relatively high hole mobility originated from the tin vacancy. The preparation of p-type SnO is a major topic for thin-film

transistors.^[25] There are both Sn²⁺ and Sn⁴⁺ inside the SnO_x film during the synthesis and coating process.^[26] It has been reported that during the synthesis of SnO_x, the SnO content in either sputtering deposition process or solution process can be easily controlled. For example, in the hydrothermal synthesis of SnO_x from SnCl₂ precursor, an O₂-deficient atmosphere leads to p-type SnO dominated products.^[26b] Using sputtering deposition, a slight change of sputtering power may change the as-prepared thin film from n-type to p-type.^[27] When changing the reactive environment from Ar gas to H₂ gas, the SnO concentration also increases.^[26a] For high performance solar cells based on SnO₂ ETL, an intrinsic n-type SnO₂ is needed, with controlled composition, morphology, and optical/electronic properties. A minimal amount of SnO inside the SnO_x is critical for high performance perovskite solar cell devices.

2.1. SnO₂ Deposition Condition

Figure 1a is a schematic drawing showing the sputtering deposition process performed in this work and details can be found in the Experimental Section. The plasma deposition may influence the bottom layer structure and also the deposited layers, which is similar to the previous report on the conventional silicon photovoltaics.^[28] For example, when depositing amorphous a-Si:H on SnO₂ by plasma enhanced chemical vapor deposition, the plasma takes away some oxygen from SnO₂ surface and deteriorates its optical/electronic properties, which decreases the junction performance in a-Si:H solar cells.^[29] This induced damage can also be observed from Ar plasma treated SnO₂.^[30] As shown in Figure 1b and Figure S1a (Supporting Information) clear gap states develop at a binding energy at around 2.6 eV. The gap states can also develop under vacuum annealing, or other reducing environment.^[31] For example, it has been reported that these gap states can form for annealing temperatures above 600 K.^[32] These gap states are associated with Sn-5s electrons that become occupied as the surface reduces to form a Sn²⁺ surface layer.^[32] As shown in Figure 1c, the formation of the gap states weakens the hole blocking properties of SnO₂ ETL and leads to increased recombination.

2.1.1. Deposition Power

To lower or eliminate the undesirable effect of Ar plasma sputtering deposition on SnO₂, it is helpful to use the minimum Ar sputtering treatment, which is achieved by adjusting the sputtering power, deposition time and O₂/Ar gas ratio. As a starting point, we first study how the deposition rate of the film will influence the film quality. The deposition rate is determined by the sputtering power. A slow deposition is necessary for depositing uniform and smooth SnO₂ films, which is also important for perovskite solar cell devices. More importantly, a higher deposition rate requires a higher power, which can induce more defect states.^[33] For SnO₂ films deposited with different rates, the film thickness is kept to be constant (35 nm) by adjusting the deposition time accordingly. The condition of 90% O₂ reactive environment was used to minimize the Ar⁺ sputtering effect. The composition of the thin film surface with a similar thickness

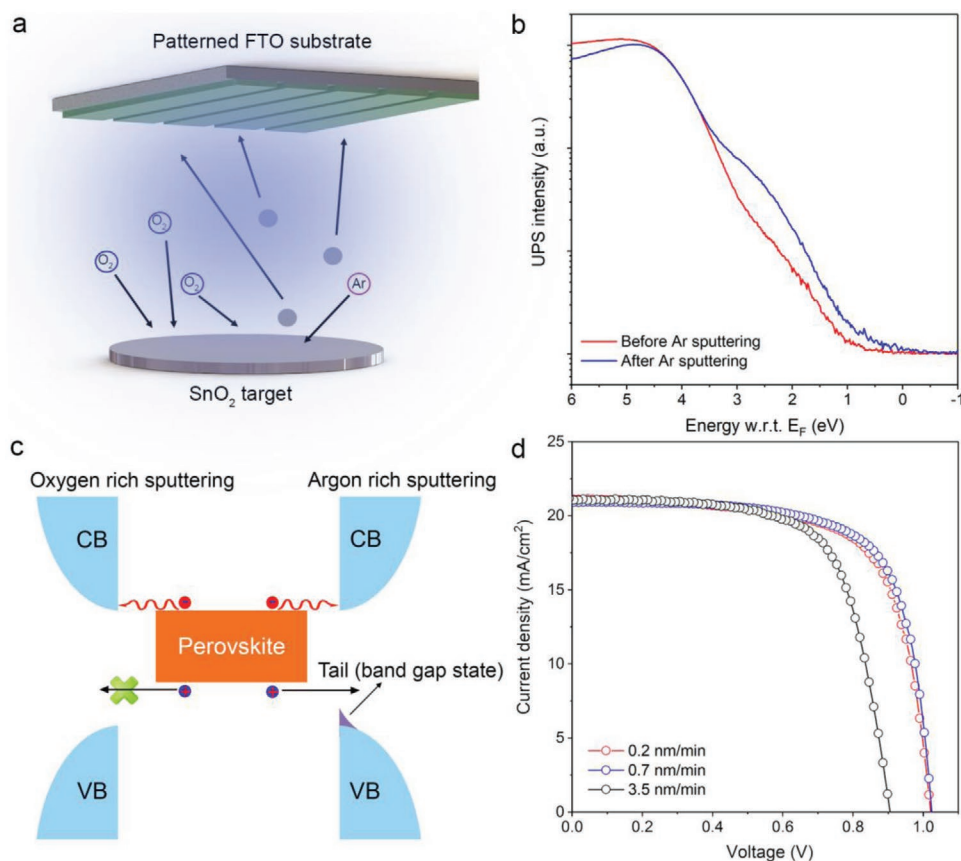


Figure 1. Structure and performance of sputtered SnO_2 films with different argon sputtering power. a) Schematic drawing showing the sputtering deposition process. b) UPS spectra (y axis in log scale) showing the valance band of SnO_2 before and after 4 kV Ar sputtering process for 30 s. c) The energy diagram that illustrates the principle of suppressing surface charge recombination by reducing the tail states that are caused by strong Ar sputtering. d) Typical J - V curves of the devices fabricated using different deposition rates of SnO_2 .

of 35 nm has been characterized by X-ray photoelectron spectroscopy (XPS). As shown in Figure S2 (Supporting Information) the core levels of Sn $3d_{5/2}$ and O 1s confirm that there is no Sn^{2+} in the as-deposited SnO_2 films. For the fluorine-doped tin oxide (FTO) substrate, the Sn $3d_{5/2}$ can be fitted into two peaks at 486.8 and 487.3 eV, which can be ascribed to Sn-O and Sn-F, respectively.^[34] The slowly deposited SnO_2 thin films show a core level of Sn $3d_{5/2}$ exhibiting a symmetric shape with a centered peak at 486.8 eV, which can be assigned to Sn^{4+} , and no Sn^{2+} is observed (485.9 eV).^[26a,c] For O 1s there are two peaks with one at 530.6 eV assigned to O- Sn^{4+} , and the other at 531.8 eV assigned to adsorbed oxygen species such as the hydroxyl group (-OH). No O- Sn^{2+} peak at 529.8 eV is observed.^[26c,35] However, in Figure S2a (Supporting Information) for a 35 nm thick SnO_2 film deposited with a higher rate we can still observe the substrate signal. The Sn $3d_{5/2}$ core level shifts to a higher binding energy and close to the substrate FTO Sn $3d_{5/2}$. As shown in Figure S3 (Supporting Information) atomic force microscopy (AFM) images of SnO_2 films deposited with a rate of 0.7 and 3.5 nm min^{-1} show different surface roughness. With a slower deposition rate (0.7 nm min^{-1}), the root mean square (RMS) roughness is smaller (25 ± 2 nm) than faster deposition (28 ± 2 nm), and also lower than the FTO substrate (28 ± 2 nm).

The sputtered SnO_2 films show high transmittance in the visible light region, with an optical bandgap of ≈ 3.99 eV (Figure S4,

Supporting Information). These properties make SnO_2 a promising ETL to replace TiO_2 . Perovskite solar cell devices based on these sputtered SnO_2 films have been fabricated. The typical perovskite material $\text{CH}_3\text{NH}_3\text{PbI}_3$ (MAPbI_3) is used in this work to evaluate the SnO_2 properties. We used a planar structure as shown in Figure S5 (Supporting Information). We can observe from Figure 1d that the device performance with a slower deposition rate is better. The V_{OC} for devices with a slower deposition rate is much higher, which can be due to the high coverage and less defect states above the valance band maximum (Table S1, Supporting Information).

2.1.2. SnO_2 Thickness

Second we study the effect of the SnO_2 film thickness by using different sputtering time. With a thickness increasing from 0 to 10 nm using a deposition rate of 0.7 nm min^{-1} , the SnO_2 film could fully cover the FTO substrate. No substrate signal is observed for the Sn $3d_{5/2}$ core level (Figure S6a, Supporting Information). As the SnO_2 film thickness increases, V_{OC} keeps decreasing (Figure S6b and Table S2, Supporting Information). In addition, the fill factor first increases, due to the better selective charge extraction and transport, and then decreases due to the increased resistance. To deposit a film with an increased

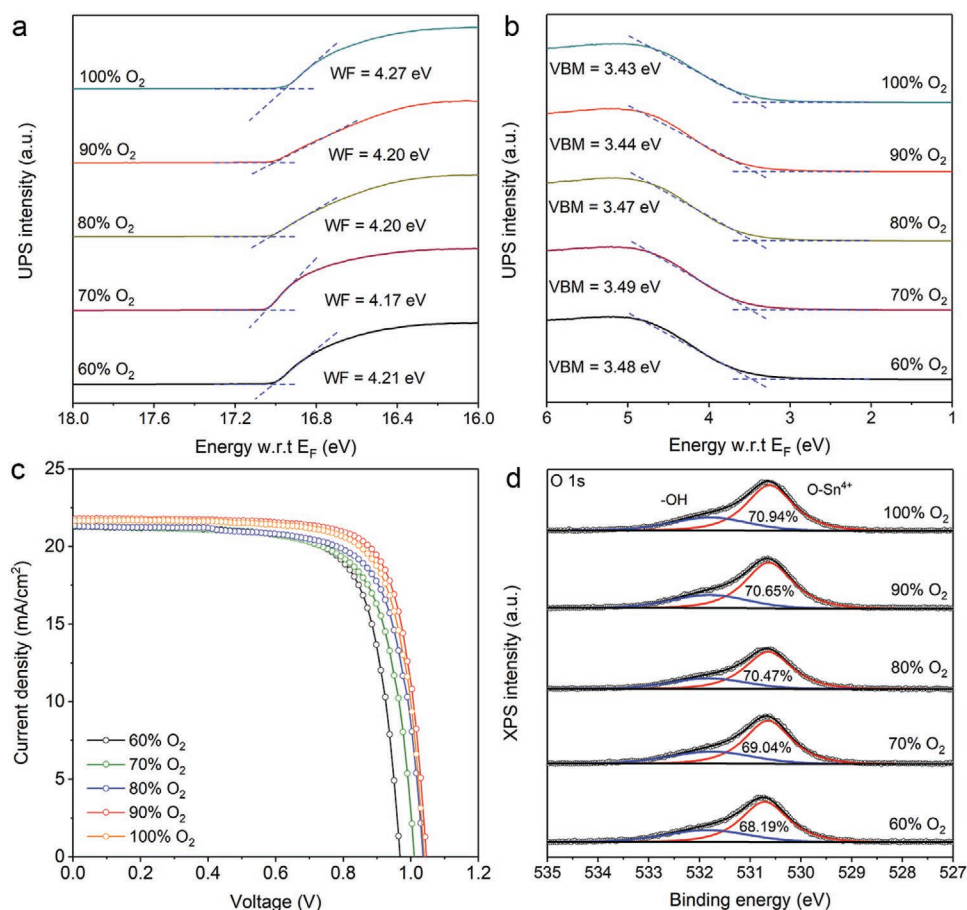


Figure 2. Electronic properties and performance of SnO₂ films deposited with different reactive environment. a) Work function of SnO₂ films deposited with different oxygen ratio. b) Valance band of SnO₂ films deposited with different oxygen ratio. c) *J*–*V* curves of MAPbI₃ devices based on the SnO₂ films deposited with different oxygen ratio. d) XPS O 1s core level of the SnO₂ films deposited with different oxygen ratio.

thickness, longer sputtering time is required. The decreased V_{OC} upon thickness increase is likely a result of the prolonged exposure to Ar⁺ plasma, which has been reported to affect the surface properties of SnO₂ films.^[36] The sputtering process can help clean deposited SnO₂ film surface with less adsorbed oxygen groups (Figure S6c, Supporting Information).^[36] However, prolonged Ar⁺ plasma exposure can also induce gap states above the valance band (Figure S6d, Supporting Information). The best performing devices are obtained using the SnO₂ film with a thickness of 17 nm, showing the highest fill factor and the second highest V_{OC} among all devices in this study (Table S2, Supporting Information). Therefore, we propose that using a sputtering process, the SnO₂ ETL with a thickness of ≈17 nm is optimal.

2.1.3. Oxidizing Environment

To further reduce the gap states, the oxidizing environment (characterized by the ratio between O₂ and Ar) is varied. It is difficult to observe the electronic structure difference in the valance band from UPS for SnO₂ with different reactive environments (Figure 2a,b). However, the device performance is consistent with the increasing oxygen ratio for sputtering (Figure 2c). The increase of fill factor is also consistent with the report that

decreasing Ar ratio during sputtering results in a lower resistance for the SnO₂ film.^[33a] When the oxygen ratio is over 90% the devices show the highest performance and not much difference is observed with an even higher oxygen ratio (Table S3, Supporting Information). To better understand the device performance difference and the chemical bonding of the films, we analyzed the O 1s peaks by peak fitting. The individual peaks at lower and higher binding energies are originated from the lattice oxygen atoms in a fully coordinated environment (Sn–O–Sn), and the hydroxide species (Sn–OH), respectively.^[35] Here we show that when increasing the O₂ content during sputtering, the –OH associated peak decreased on the SnO₂ surface, as illustrated in Figure 2d. The peak corresponding to the Sn–O–Sn backbones, which serves as electron conduction pathways, is more prominent under the higher oxygen ratio deposition condition, and the peak corresponding to Sn–OH, playing a role as shallow trap sites, is slightly weaker under the higher oxygen ratio condition.^[37] The extensive presence of Sn–OH is due to incomplete oxidation of the oxide lattice, which decreases the mobility of SnO₂ and hinders electron transport and/or lowers hole blocking property.^[38] The decreasing of –OH could also help enhance charge extraction and is consistent with the time resolved photoluminescent (TRPL) spectra (Figure S7 and Table S4, Supporting Information). The resulting curves

are fitted by a double exponential model with a fast and slow photoluminescence decay time constants (τ_1 and τ_2).^[39] The fast decay time constant τ_1 corresponds to the quenching of charge carriers by electron extraction from MAPbI₃ to SnO₂.^[40] With the increasing of oxygen ratio in the reactive environment, the fast time constant decreased from 4.6 ± 0.3 ns for MAPbI₃ on FTO to 3.7 ± 0.2 ns for MAPbI₃ on SnO₂ deposited with oxygen ratio higher than 80%. While in a mild or low oxidizing environment, the deposited SnO₂ film only shows slightly improved electron extraction properties (slightly decreased τ_1) compared with FTO substrate. This observation also implies that a higher oxygen ratio reactive environment could help deposit SnO₂ with higher quality for charge extraction.

2.1.4. SnO₂ Crystallinity

To improve the quality of sputtered SnO₂ films, the film crystallinity has been investigated. Typically room temperature sputtered SnO₂ films comprise nanometer-sized crystals embedded in an amorphous matrix.^[33b] One way to improve the quality of SnO₂ film is to perform post annealing, which

can help improve the crystallinity, mobility, and carrier density.^[41] As shown in Figure S8 (Supporting Information), when the temperature is higher than 300 °C, the (110), (101), (220), and (211) peaks are observed.^[10a] The crystallinity improves as the annealing temperature is further increased to 500 °C. However, although we expect higher performance with mild post annealing, the devices performance keeps decreasing with increasing annealing temperature (Figure S9 and Table S5, Supporting Information). As we can see from the AFM images of SnO₂ with different annealing temperature in Figure S10 (Supporting Information) the RMS roughness on average is around 25 nm before and after annealing, thus the morphology might not be the main cause for inferior performance. Annealing of SnO₂ films can introduce a variety of changes in the films, such as carrier density change, unbalanced charge transport between ETL/perovskite and hole transport layer/perovskite, structural imperfections, disruption of ordering, sub-nanometer crystallinity, and surface roughness.^[41] We propose that the decreased performance is a result of one or a combination of several of the factors mentioned above. Here we show that room temperature sputtering deposition of SnO₂ without post annealing shows the best performance.

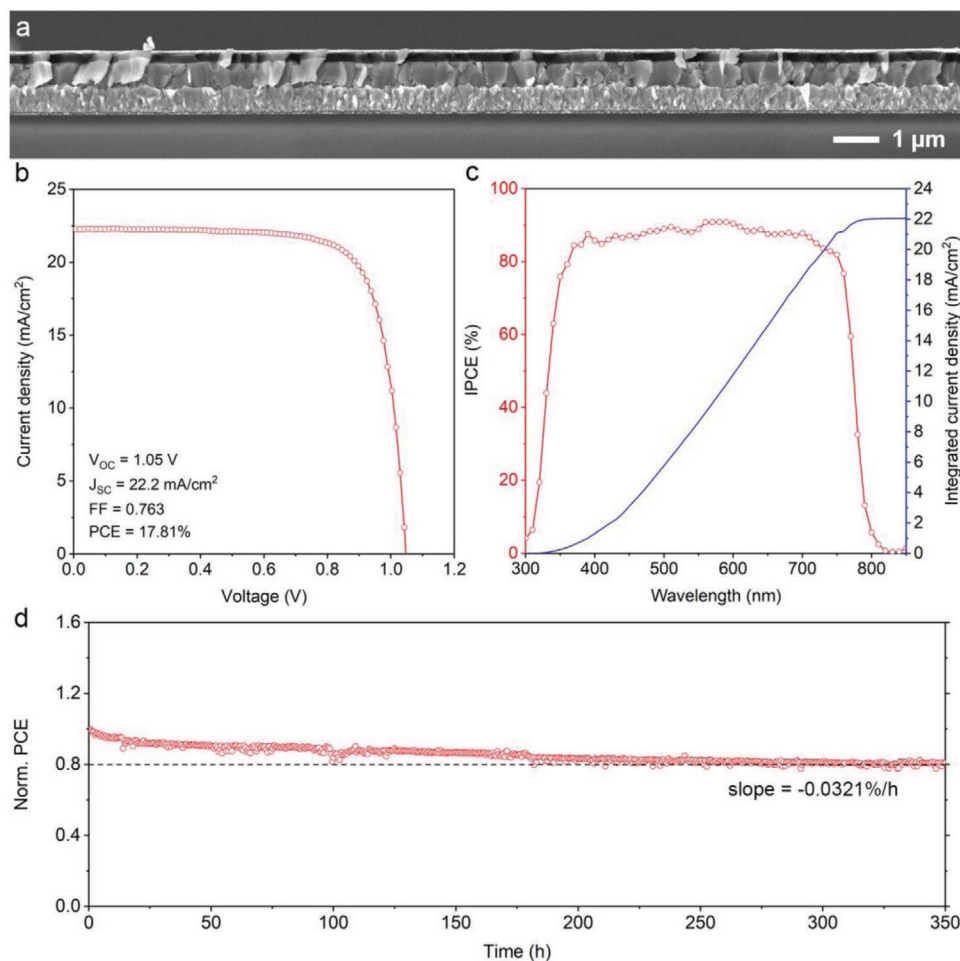


Figure 3. Perovskite solar cell device performance. a) Cross-section SEM of perovskite solar cell. b) J - V curve and c) EQE and related integrated current density of the champion device based on the sputtered SnO₂ ETL and MAPbI₃. d) The plot of normalized PCE as a function of operation time to evaluate the stability of solar cell under continuous light illumination.

2.2. Perovskite Solar Cells and Modules

2.2.1. Small Area Cells and Operational Stability

The cross-section image of the solar cell device in **Figure 3a** demonstrates the high quality and uniform fabrication of the device. With the optimization of the morphology, composition, and surface properties of sputtered SnO₂, an efficiency of 17.8% has been obtained for planar junction device based on MAPbI₃ (**Figure 3b**). Compared with our previous developed room temperature sputtered TiO₂ ETL (PCE 16.4 ± 0.7%), the cells based on the SnO₂ (PCE 16.7 ± 0.5%) ETL shows better performance, as a result of the higher conductivity, larger carrier mobility, and smaller thickness.^[8a] SnO₂ has high transmittance in visible light region (**Figure S3**, Supporting Information) and a deep valence band, which helps better block the hole, and decrease recombination at the SnO₂/perovskite interface (**Figure 2b**). The high J_{SC} of 22.2 mA cm⁻² is consistent with incident photon-to-electron conversion efficiency (IPCE) integrated J_{SC} of 22.0 mA cm⁻², which also confirms the high transmittance of the SnO₂ layer.

Another advantage of the SnO₂ based perovskite solar cells when compared with TiO₂ is the higher operational stability and longer lifetime. In our previous study the planar structure perovskite solar cell devices based on sputtered TiO₂ show a T₈₀ lifetime less than 100 h, and the lifetime is even shorter when using crystalline TiO₂ ETL due to enhanced photocatalytic properties of TiO₂.^[8a] The lifetime could reach 250 h, after an interface modification process, which inevitably adds up the complexity of the fabrication process.^[8a] Here the operational lifetime of MAPbI₃ solar cell based on SnO₂ ETL was measured under maximum power point with continuous light illumination, under 45 °C (**Figure 3d**). This protocol is also considered to be the most reliable way to test operational stability.^[42] Two stages are observed for the performance degradation, with the initial “burn-in” exponential loss followed by a linear one.^[42] With considering the initial exponential losses, the best T₈₀ lifetime reaches 350 h with the average lifetime over 200 h (**Figure S11**, Supporting Information), which is substantially longer than the lifetime of perovskite solar cells based on sputtered TiO₂ ETL reported in our previous paper.^[8a] If we make extrapolations disregarding the (potentially reversible) initial exponential losses, the T₈₀ lifetime reaches 625 h with the linear slope of -0.0321% h⁻¹.^[42] Also the initial “burn-in” process is short which is consistent with a recent report that compares solution deposited SnO₂ and TiO₂.^[11] However even for SnO₂ based planar junction devices there still exist hysteresis (**Figure S12**, Supporting Information) and further interface modification or change of perovskite materials may help eliminate this effect.^[17,19,41,43]

Due to the mismatch of the energy level between SnO₂ and MAPbI₃ (**Figures S13–15**, Supporting Information), the performance of sputtered SnO₂ based devices is lower than expectation. To make full use of this low temperature sputtered SnO₂ as high performance ETL, a recently reported mixed perovskite Cs_{0.06}MA_{0.27}FA_{0.67}PbI_{2.7}Br_{0.3} solar cell has shown better energy level alignment and smaller bandgap (1.55 eV) (**Figure S14**, Supporting Information).^[10b,44] Due to improved energy level alignment, V_{OC} is improved from 1.04 to 1.08 V compared with MAPbI₃. Also the hysteresis is decreased (**Figure S16**,

Supporting Information). A hero device showed reverse scan efficiency of 20.2% and stabilized power output of 19.8% (**Figure 4a,b**). With a smaller bandgap J_{SC} is improved up to 22.8 mA cm⁻² from IPCE data (**Figure 4c**). Due to the uniform sputtering process, the reproducibility is high, with all the devices show performance over 18% (**Figure 4d**).

2.2.2. Perovskite Solar Modules and Operational Stability

Sputtering deposition is promising for large scale module fabrication. Sputtering is an industry compatible process for large scale and uniform film deposition. Here PSMs with a geometric fill factor of 91% have been fabricated as shown in **Figure 5a** and **Figure S17** (Supporting Information). In a 5 cm × 5 cm substrate, there are six sub-cells in series connection. Between each cell there is a 200 μm width line (P1) patterned by laser to separate FTO stripes, with a dimension of 7.75 mm by 49 mm (**Figure S17**, Supporting Information). After coating SnO₂, perovskite and spiro-MeOTAD, one more line (P2) with a width of 200 μm is patterned by CO₂ laser to expose the bottom FTO electrodes to form the series connections between the cells. For P2 cutting, the laser wavelength and energy need be fine controlled to only remove the top layer but keep the FTO layer undamaged.^[15] However this process requires a more complicated laser system. Without removing the bottom ETL such as TiO₂ will significantly increase the series resistance thus lower the performance when scaling up to a module.^[16] By using SnO₂ here the P2 process is easier to control. SnO₂ shows ten times higher conductivity (1.7 × 10⁻³ S cm⁻¹) than TiO₂ (10⁻⁴ S cm⁻¹). The sheet resistance of transparent conductive electrode with ultrathin (≈17 nm) SnO₂ films increases only slightly from 7.1 to 7.3 Ω/□, while between the FTO stripes there is still infinite resistance. All these factors contribute to a lower laser patterning energy from a simple CO₂ laser system. After evaporating gold electrodes, each cell is separated by cutting with a knife to form P3 patterning. The PSMs with an aperture area of 22.8 cm² show a best efficiency of 12.03% (**Figure 5b**), with an average efficiency of 10.8% (**Table S6**, Supporting Information). Consistent with small area cells, the T₈₀ operational lifetime of the solar module reaches 515 h, with a decay rate of 0.0388% h⁻¹ for PCE (**Figure 5c**). These results show that sputtered SnO₂ is promising for high stability efficient solar cells/modules.

3. Conclusion

In summary, the structure and properties of sputtered SnO₂ films have been studied. In a highly oxidized reactive environment, high quality SnO₂ films have been fabricated. By minimizing Ar in the reactive environment the gap state is minimized. Also surface absorbed oxygen groups are reduced. With the optimized morphology and surface structure of SnO₂ ETL, perovskite solar cells exhibit an efficiency of 20.2%. In addition, this high quality SnO₂ ETL is promising for large scale perovskite solar modules. As a demonstration, PSMs with aperture area of 22.8 cm² and six cells in series connection are fabricated and show an efficiency over 12%. To summarize, sputtering

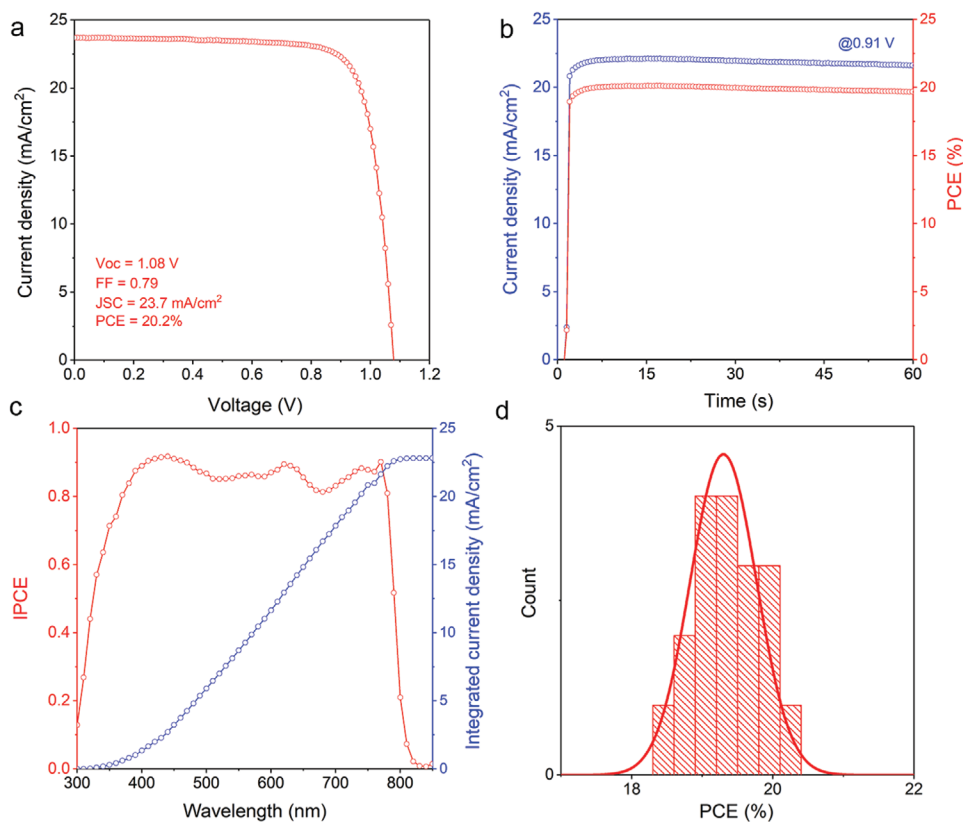


Figure 4. Device performance for the perovskite solar cells based on the mixed perovskite. a) J - V scan, b) maximum power point output, and c) EQE of the champion device based on the sputtered SnO_2 ETL and $\text{Cs}_{0.06}\text{MA}_{0.27}\text{FA}_{0.67}\text{PbI}_{2.7}\text{Br}_{0.3}$. d) Statistical performance data of devices based on the sputtered SnO_2 ETL and $\text{Cs}_{0.06}\text{MA}_{0.27}\text{FA}_{0.67}\text{PbI}_{2.7}\text{Br}_{0.3}$.

SnO_2 is a cost-effective, efficient electron transport material for high stability efficient perovskite solar cells/modules towards commercialization.

4. Experimental Section

Preparation of SnO_2 Films: SnO_2 was deposited by sputtering (Vacuum Sputter Deposition System, CAM-S, ULVAC). The SnO_2 (4 N, Furuuchi Chemical) was deposited in a condition of 10 sccm O_2/Ar mixture with a power of 60 W for 25 min. An oxygen-rich condition is necessary to ensure that the majority of Sn in the film is Sn^{4+} , while argon gas is typically required for plasma triggering. The oxygen ratio of 70%, 80%, 90%, and 100% were used while keeping the pressure inside the sputtering chamber at around 0.2 Pa. For different deposition rate, 40, 60, and 100 W were applied while keeping the deposition film with a thickness of 35 nm. Although even slower deposition rates might give better coverage, the time should also be considered. Here a deposition rate of 0.7 nm min^{-1} (60 W) is chosen for further properties investigation. This sputtering deposition is promising for conformal coating.

Solar Cell/Module Fabrication: The glass/FTO with sheet resistance $\approx 7 \Omega/\square$ (OPVT) was sequentially washed with 1 wt% sodium dodecyl sulfate aqueous, deionized water, acetone, and isopropanol. After deposition of electron transport layer, the substrate was under UV-Ozone treatment for 15 min before use. For antisolvent deposition process, the solution of MAPbI_3 (1.2 M) was made by mixing PbI_2 (TCI) and MAI (Dyesol) into a dimethylformamide (DMF) and dimethyl sulfoxide (DMSO) mixed solvent ($v/v = 7/1$). For the MAPbI_3 layer, the solution was cast onto substrates and spin coated at 2800 rpm for 25 s. After 7 s of spinning,

200 μL of diethyl ether was drop cast onto the film. The MAPbI_3 film was formed after annealing at 100°C for 30 min in a 5% humidity box. For $\text{Cs}_{0.06}\text{MA}_{0.27}\text{FA}_{0.67}\text{PbI}_{2.7}\text{Br}_{0.3}$, a two-step coating process was applied as reported.^[44] First 1.3 M PbI_2/CsI (6%) DMF solution was spin coated inside glovebox. After annealing at 80°C for 10 min the substrates were cooled down. Then MAI/FAI/MABr/MACl (20 mg/40 mg/5 mg/5 mg in 1 mL IPA) solution was cast on the substrate and spin coated. The mixed perovskite film was formed by annealing in air. For solar cell fabrication, a hole transport material solution (72.5 mg mL^{-1} of spiro-MeOTAD (2,2',7,7'-tetrakis (N,N -di-*p*-methoxyphenylamine)-9,9-spirobifluorene), 17 $\mu\text{L mL}^{-1}$ of lithium bis(trifluoromethylsulfonyl) imide solution (520 mg mL^{-1} in acetonitrile) and 28.75 $\mu\text{L mL}^{-1}$ of 4-*tert*-butylpyridine in chlorobenzene) was spin coated at 3000 rpm for 30 s on top of MAPbI_3 film. Finally, an 80 nm thick Au film was deposited to complete the solar cell. For module fabrication, after coating spiro-MeOTAD the modules were patterned by a CO_2 laser cutter to expose the bottom FTO electrode for series connection. After deposition of 120 nm thick Au the substrate was cut by a fine controlled blade to separate each cells.

Characterization: The thickness of the amorphous SnO_2 layer and perovskite active layer was measured with a surface profiler (Bruker Dektak XT). The transmittance and absorbance spectra were measured with a UV-vis spectrometer (Jasco V-670). The surface morphology was performed in an atomic force microscope (Asylum). The UPS and XPS spectra were recorded from an X-ray photoelectron spectrometer (XPS-AXIS Ultra HAS, Kratos) equipped with monochromatic $\text{Al-K}\alpha = 1486.6 \text{ eV}$ and nonmonochromatic $\text{He-I} = 21.22 \text{ eV}$ sources. UV and X-ray induced sample damage was monitored by taking five consecutive scans and by comparing these spectra. Crystal structure of SnO_2 was characterized with an X-ray diffractometer (XRD) (Bruker D8 Discover). J - V curves were recorded by a Keithley 2420 Source Meter under illumination (100 mW cm^{-2})

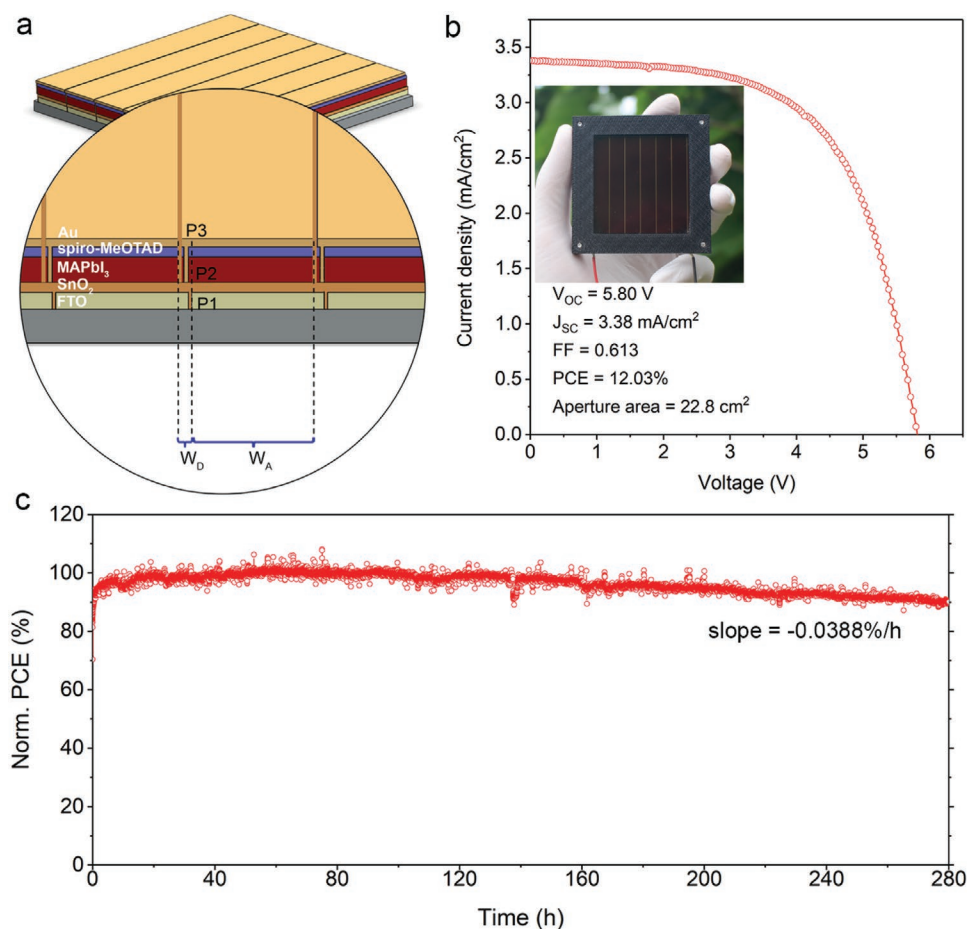


Figure 5. Perovskite solar module with sputtered SnO_2 ETL. a) Schematic drawing showing perovskite solar module structure. b) J - V curve of perovskite solar module (the inset shows the optical image of our perovskite solar module). c) The plot of normalized PCE as a function of operation time to evaluate lifetime of the solar module under continuous light illumination.

of simulated AM1.5 solar light coming from a solar simulator (Oriental Sol1A equipped with a 350 W Xe lamp and an AM1.5 filter). The light intensity was calibrated using a reference Si solar cell. The effective area of 0.09 cm^2 for small cells was defined by an aperture. For stability measurements, the devices were connected to a load resistance of 180Ω and every 30 min a current-voltage scan was operated for each cell by sweeping the voltage from reverse to forward bias conditions (forward sweep) then forward to reverse bias conditions (reverse) with a scan rate of 50 mV s^{-1} . A homemade program was used to record current-voltage scan every 30 min. No UV-filters were used, i.e., the UV component was included while under illumination. The stability measurement was performed in a nitrogen box with a maximum RH of 5%. The EQE spectra were characterized by an IPCE measurement system (Oriental IQE 200).

OIST Proof of Concept (POC) Program, the OIST R&D Cluster Research Program, and JSPS KAKENHI Grant Number JP18K05266. The authors would like to thank OIST Mech. Eng. & Microfabrication Support Section for maintenance of cleanroom and sputtering equipment.

Conflict of Interest

The authors declare no conflict of interest.

Keywords

electron transport layer, perovskite solar modules, scalability, sputtered SnO_2 , stability

Supporting Information

Supporting Information is available from the Wiley Online Library or from the author.

Acknowledgements

L.Q. and Z.L. contributed equally to this work. This work was supported by funding from the Energy Materials and Surface Sciences Unit of the Okinawa Institute of Science and Technology Graduate University, the

Received: September 25, 2018
Revised: November 10, 2018
Published online: December 13, 2018

- [1] a) M. A. Green, Y. Hishikawa, E. D. Dunlop, D. H. Levi, J. Hohl-Ebinger, A. W. Y. Ho-Baillie, *Prog. Photovoltaics* **2018**, *26*, 3; b) Best Research-Cell Efficiencies, <https://www.nrel.gov/pv/assets/images/efficiency-chart-20180716.jpg>, (accessed: July 16th).
[2] L. Qiu, L. K. Ono, Y. B. Qi, *Mater. Today Energy* **2018**, *7*, 169.

- [3] a) E. J. Juarez-Perez, Z. Hawash, S. R. Raga, L. K. Ono, Y. B. Qi, *Energy Environ. Sci.* **2016**, *9*, 3406; b) J. Yang, B. D. Siempelkamp, D. Liu, T. L. Kelly, *ACS Nano* **2015**, *9*, 1955; c) S. Wang, Y. Jiang, E. J. Juarez-Perez, L. K. Ono, Y. B. Qi, *Nat. Energy* **2017**, *2*, 16195.
- [4] a) J. Yang, B. D. Siempelkamp, E. Mosconi, F. De Angelis, T. L. Kelly, *Chem. Mater.* **2015**, *27*, 4229; b) Y. Dkhissi, S. Meyer, D. Chen, H. C. Weerasinghe, L. Spiccia, Y. B. Cheng, R. A. Caruso, *ChemSusChem* **2016**, *9*, 687.
- [5] L. K. Ono, S. R. Raga, M. Remeika, A. J. Winchester, A. Gabe, Y. B. Qi, *J. Mater. Chem. A* **2015**, *3*, 15451.
- [6] a) Y. Kato, L. K. Ono, M. V. Lee, S. Wang, S. R. Raga, Y. B. Qi, *Adv. Mater. Interfaces* **2015**, *2*, 1500195; b) K. Domanski, J.-P. Correa-Baena, N. Mine, M. K. Nazeeruddin, A. Abate, M. Saliba, W. Tress, A. Hagfeldt, M. Grätzel, *ACS Nano* **2016**, *10*, 6306.
- [7] C. Manspeaker, S. Venkatesan, A. Zakhidov, K. S. Martirosyan, *Curr. Opin. Chem. Eng.* **2017**, *15*, 1.
- [8] a) L. Qiu, L. K. Ono, Y. Jiang, M. R. Leyden, S. R. Raga, S. Wang, Y. B. Qi, *J. Phys. Chem. B* **2018**, *122*, 511; b) N. Ahn, K. Kwak, M. S. Jang, H. Yoon, B. Y. Lee, J.-K. Lee, P. V. Pikhitsa, J. Byun, M. Choi, *Nat. Commun.* **2016**, *7*, 13422.
- [9] a) Q. Jiang, Z. Chu, P. Wang, X. Yang, H. Liu, Y. Wang, Z. Yin, J. Wu, X. Zhang, J. You, *Adv. Mater.* **2017**, *29*, 1703852; b) D. Yang, R. Yang, K. Wang, C. Wu, X. Zhu, J. Feng, X. Ren, G. Fang, S. Priya, S. Liu, *Nat. Commun.* **2018**, *9*, 3239.
- [10] a) Q. Jiang, L. Zhang, H. Wang, X. Yang, J. Meng, H. Liu, Z. Yin, J. Wu, X. Zhang, J. You, *Nat. Energy* **2017**, *2*, 16177; b) J. P. Correa Baena, L. Steier, W. Tress, M. Saliba, S. Neutzner, T. Matsui, F. Giordano, T. J. Jacobsson, A. R. Srimath Kandada, S. M. Zakeeruddin, A. Petrozza, A. Abate, M. K. Nazeeruddin, M. Grätzel, A. Hagfeldt, *Energy Environ. Sci.* **2015**, *8*, 2928.
- [11] J. A. Christians, P. Schulz, J. S. Tinkham, T. H. Schloemer, S. P. Harvey, B. J. Tremolet de Villers, A. Sellinger, J. J. Berry, J. M. Luther, *Nat. Energy* **2018**, *3*, 68.
- [12] a) Y. Jiang, M. R. Leyden, L. Qiu, S. Wang, L. K. Ono, Z. Wu, E. J. Juarez-Perez, Y. B. Qi, *Adv. Funct. Mater.* **2018**, *28*, 1703835; b) M. R. Leyden, Y. Jiang, Y. B. Qi, *J. Mater. Chem. A* **2016**, *4*, 13125; c) M. Yang, Z. Li, M. O. Reese, O. G. Reid, D. H. Kim, S. Siol, T. R. Klein, Y. Yan, J. J. Berry, M. F. A. M. van Hest, K. Zhu, *Nat. Energy* **2017**, *2*, 17038; d) Z. Li, T. R. Klein, D. H. Kim, M. Yang, J. J. Berry, M. F. A. M. van Hest, K. Zhu, *Nat. Rev. Mater.* **2018**, *3*, 18017.
- [13] H. Chen, F. Ye, W. Tang, J. He, M. Yin, Y. Wang, F. Xie, E. Bi, X. Yang, M. Grätzel, L. Han, *Nature* **2017**, *550*, 92.
- [14] B. Ding, S.-Y. Huang, Q.-Q. Chu, Y. Li, C.-X. Li, C.-J. Li, G.-J. Yang, *J. Mater. Chem. A* **2018**, *6*, 10233.
- [15] A. L. Palma, F. Matteocci, A. Agresti, S. Pescetelli, E. Calabrò, L. Vesce, S. Christiansen, M. Schmidt, A. D. Carlo, *IEEE J. Photovoltaics* **2017**, *7*, 1674.
- [16] M. Yang, D. H. Kim, T. R. Klein, Z. Li, M. O. Reese, B. J. Tremolet de Villers, J. J. Berry, M. F. A. M. van Hest, K. Zhu, *ACS Energy Lett.* **2018**, *3*, 322.
- [17] W. Ke, G. Fang, Q. Liu, L. Xiong, P. Qin, H. Tao, J. Wang, H. Lei, B. Li, J. Wan, G. Yang, Y. Yan, *J. Am. Chem. Soc.* **2015**, *137*, 6730.
- [18] J.-Y. Chen, C.-C. Chueh, Z. Zhu, W.-C. Chen, A. K. Y. Jen, *Solar Energy Mater. Solar Cells* **2017**, *164*, 47.
- [19] C. Xiao, C. Wang, W. Ke, B. P. Gorman, J. Ye, C.-S. Jiang, Y. Yan, M. M. Al-Jassim, *ACS Appl. Mater. Interfaces* **2017**, *9*, 38373.
- [20] E. H. Anaraki, A. Kermanpur, L. Steier, K. Domanski, T. Matsui, W. Tress, M. Saliba, A. Abate, M. Grätzel, A. Hagfeldt, J.-P. Correa-Baena, *Energy Environ. Sci.* **2016**, *9*, 3128.
- [21] J. Ma, X. Zheng, H. Lei, W. Ke, C. Chen, Z. Chen, G. Yang, G. Fang, *Sol. RRL* **2017**, *1*, 1700118.
- [22] H. Tao, Z. Ma, G. Yang, H. Wang, H. Long, H. Zhao, P. Qin, G. Fang, *Appl. Surf. Sci.* **2018**, *434*, 1336.
- [23] F. Ali, N. D. Pham, J. Bradford, N. Khoshshiraf, K. Ostrikov, J. Bell, H. Wang, T. Tesfamichael, *ChemSusChem* **2018**, *11*, 3096.
- [24] K. G. Godinho, A. Walsh, G. W. Watson, *J. Phys. Chem. C* **2009**, *113*, 439.
- [25] H. Yabuta, N. Kaji, R. Hayashi, H. Kumomi, K. Nomura, T. Kamiya, M. Hirano, H. Hosono, *Appl. Phys. Lett.* **2010**, *97*, 072111.
- [26] a) P. C. Hsu, C. J. Hsu, C. H. Chang, S. P. Tsai, W. C. Chen, H. H. Hsieh, C. C. Wu, *ACS Appl. Mater. Interfaces* **2014**, *6*, 13724; b) J. Wang, H. Li, S. Meng, X. Ye, X. Fu, S. Chen, *RSC Adv.* **2017**, *7*, 27024; c) H. Luo, L. Y. Liang, H. T. Cao, Z. M. Liu, F. Zhuge, *ACS Appl. Mater. Interfaces* **2012**, *4*, 5673.
- [27] Y. Li, Q. Xin, L. Du, Y. Qu, H. Li, X. Kong, Q. Wang, A. Song, *Sci. Rep.* **2016**, *6*, 36183.
- [28] H. Schade, Z. E. Smith, J. H. Thomas, A. Catalano, *Thin Solid Films* **1984**, *117*, 149.
- [29] S. S. Hegedus, *J. Appl. Phys.* **2002**, *92*, 620.
- [30] H. Y. Yu, X. D. Feng, D. Grozea, Z. H. Lu, R. N. S. Sodhi, A.-M. Hor, H. Aziz, *Appl. Phys. Lett.* **2001**, *78*, 2595.
- [31] M. Batzill, K. Katsiev, J. M. Burst, U. Diebold, A. M. Chaka, B. Delley, *Phys. Rev. B* **2005**, *72*, 165414.
- [32] M. Batzill, *Sensors* **2006**, *6*, 1345.
- [33] a) D. Leng, L. Wu, H. Jiang, Y. Zhao, J. Zhang, W. Li, L. Feng, *Int. J. Photoenergy* **2012**, *2012*, 1; b) B. S. Tosun, R. K. Feist, A. Gunawan, K. A. Mkhoyan, S. A. Campbell, E. S. Aydil, *Thin Solid Films* **2012**, *520*, 2554.
- [34] a) S. Wu, S. Yuan, L. Shi, Y. Zhao, J. Fang, *J. Colloid Interface Sci.* **2010**, *346*, 12; b) H. Liu, A. Wang, Q. Sun, T. Wang, H. Zeng, *Catalysts* **2017**, *7*, 385.
- [35] F. A. Akgul, C. Gumus, A. O. Er, A. H. Farha, G. Akgul, Y. Ufuktepe, Z. Liu, *J. Alloys Compd.* **2013**, *579*, 50.
- [36] S. Bansal, D. K. Pandya, S. C. Kashyap, *Appl. Phys. Lett.* **2014**, *104*, 082108.
- [37] K. K. Banger, Y. Yamashita, K. Mori, R. L. Peterson, T. Leedham, J. Rickard, H. Sirringhaus, *Nat. Mater.* **2011**, *10*, 45.
- [38] H. Yu, H. I. Yeom, J. W. Lee, K. Lee, D. Hwang, J. Yun, J. Ryu, J. Lee, S. Bae, S. K. Kim, J. Jang, *Adv. Mater.* **2018**, *30*, 1704825.
- [39] S. D. Stranks, G. E. Eperon, G. Grancini, C. Menelaou, M. J. P. Alcocer, T. Leijtens, L. M. Herz, A. Petrozza, H. J. Snaith, *Science* **2013**, *342*, 341.
- [40] G. Xing, N. Mathews, S. Sun, S. S. Lim, Y. M. Lam, M. Grätzel, S. Mhaisalkar, T. C. Sum, *Science* **2013**, *342*, 344.
- [41] a) C. Wang, C. Xiao, Y. Yu, D. Zhao, R. A. Awani, C. R. Grice, K. Ghimire, I. Constantinou, W. Liao, A. J. Cimaroli, P. Liu, J. Chen, N. J. Podraza, C. S. Jiang, M. M. Al-Jassim, X. Zhao, Y. Yan, *Adv. Energy Mater.* **2017**, *7*, 1700414; b) W. Ke, D. Zhao, A. J. Cimaroli, C. R. Grice, P. Qin, Q. Liu, L. Xiong, Y. Yan, G. Fang, *J. Mater. Chem. A* **2015**, *3*, 24163; c) Y. Lee, S. Lee, G. Seo, S. Paek, K. T. Cho, A. J. Huckaba, M. Calizzi, D.-w. Choi, J.-S. Park, D. Lee, H. J. Lee, A. M. Asiri, M. K. Nazeeruddin, *Adv. Sci.* **2018**, *5*, 1800130; d) K.-H. Jung, J.-Y. Seo, S. Lee, H. Shin, N.-G. Park, *J. Mater. Chem. A* **2017**, *5*, 24790.
- [42] K. Domanski, E. A. Alharbi, A. Hagfeldt, M. Grätzel, W. Tress, *Nat. Energy* **2018**, *3*, 61.
- [43] G. Yang, C. Wang, H. Lei, X. Zheng, P. Qin, L. Xiong, X. Zhao, Y. Yan, G. Fang, *J. Mater. Chem. A* **2017**, *5*, 1658.
- [44] L. Li, N. Liu, Z. Xu, Q. Chen, X. Wang, H. Zhou, *ACS Nano* **2017**, *11*, 8804.